ACS OMEGA

http://pubs.acs.org/journal/acsodf

Article

Adhesion Performance of Ettringite at the Interface with Silane and GO/Silane: Insights into Molecular Dynamics Simulations

Shaochun Li, Yuying Duan, Heping Zheng, Dongshuai Hou, Shiyu Sui, Ang Liu, and Pan Wang*

Cite This: *ACS Omega* 2023, 8, 16016−16031

Read Online

ACCESS | Metrics & More | Article Recommendations

ABSTRACT: The application of silane in sulfoaluminate cement repair materials can improve its waterproof, permeability, freeze−thaw, and other properties, but it would reduce the mechanical properties of sulfoaluminate cement-based materials, making it unable to better meet the engineering requirements and durability indices. The modification of silane with graphene oxide (GO) can effectively address this issue. However, the failure mechanism of the interface between silane and sulfoaluminate cement-based materials and the modification mechanism of GO remain unclear. In this paper, the interface-bonding mechanical models of isobutyltriethoxysilane (IBTS)/ettringite and GO-IBTS/ettringite are established by molecular dynamics method to study the source of interface-bonding properties of IBTS, GO-IBTS, and ettringite, as well as the failure mechanism of interface bonding, to reveal the mechanism of GO-modifying IBTS to improve the interface-bonding properties of IBTS and ettringite. This study finds that the bonding properties of the IBTS, GO-IBTS, and ettringite interface are derived from the amphiphilic nature of IBTS, which can only produce unilateral bonding with ettringite, thus becoming a weak link in interface dissociation. The double-sided nature of GO functional groups enables GO-IBTS to interact well with bilateral ettringite, thus enhancing the interface-bonding properties.

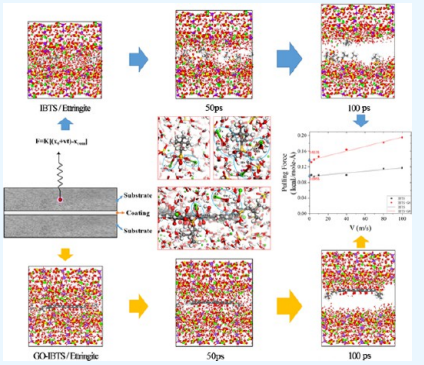

1. INTRODUCTION

Concrete has been in use for over 100 years, and owing to its abundant raw materials, simple technology, and excellent performance, it has become one of the most crucial building materials in modern engineering. In addition to the construction and transportation, water conservancy, port and other civil engineering fields, the shipbuilding industry, machinery industry, ocean development, geothermal engineering, and other related fields also have good applications.[1−4] Concrete in the process of long-term bearing,[5] subject to wind and snow erosion,[6] deicing salt corrosion,[7] especially in the dry and wet cycles of marine concrete,[8,9] chloride ion erosion,[10−12] and wave impact[13] and other multiple effects, would appear cracks, fall off, and other defects and affect the use of esthetic appearance and durability. However, the solution of large-scale demolition and construction is faced with capital consumption, material cost caused by a large amount of construction waste, and time cost caused by shutdown.[14,15] Therefore, the research on the repair problem of this kind of project has become a major topic of universal attention in the international engineering field.

Ordinary Portland cement is prone to cracking after it shrinks, which can greatly impact concrete durability, corrosion resistance, and permeability resistance. Therefore, repair engineering often chooses to use sulfoaluminate cement, which can shorten the construction time; the performance of microvolume expansion can also compensate for shrinkage, effectively improve the efficiency of construction, to prevent subsequent cracking problems. The main mineral components of sulfoaluminate cement are anhydrous calcium sulfoaluminate and dicalcium silicate, iron phase, gypsum, and mineral admixture.[16] The main hydration products are ettringite, aluminum glue, and calcium silicate hydrate gel, of which ettringite accounts for more than 50%, which is the main source of strength of sulfoaluminate cement-based materials. The durability of sulfoaluminate cement-based materials after the repair is the focus of engineering application, especially in the face of the harsh environment such as ocean and cold, where structural deterioration would occur in the form of freeze−thaw damage, chemical erosion, alkali aggregate reaction, and other factors. Therefore, researchers have used various methods to modify it, especially polymer-modified cement-based repair mortar, which can achieve a good fit and has been widely studied. The commonly modified polymers include ethyl acetate, polypropylene, and styrene butadiene emulsion, among which organosilane is favored by researchers because its hydrophilic and hydrophobic ends can produce high

Received: December 22, 2022
Accepted: April 10, 2023
Published: April 26, 2023

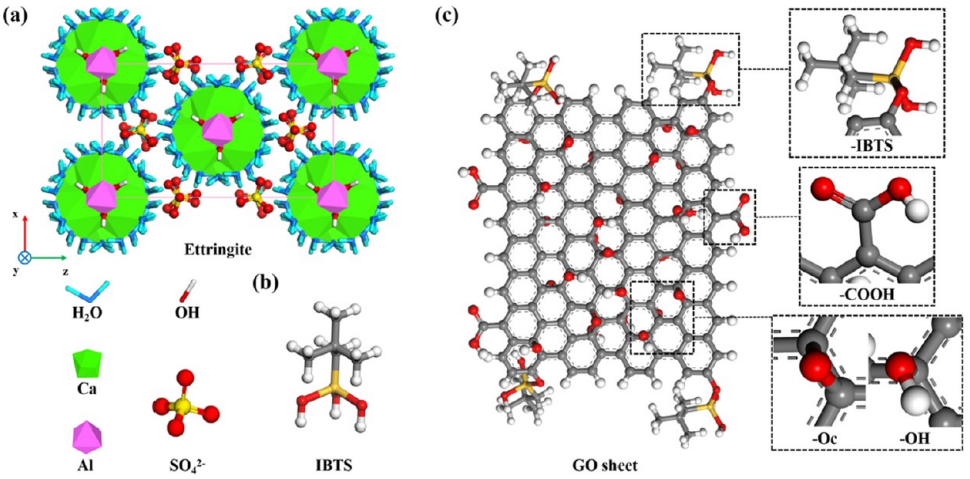

Figure 1. Initial unit cell of (a) ettringite, (b) IBTS, and (c) GO-IBTS.

plasticity. Guo et al.[17,18] found that the addition of silane-modified substances can form a network hydrophobic siloxane film on the surface of sulfoaluminate cement-based materials, which improves permeability and freezing resistance. Chen et al.[19] studied several commonly used surface treating agents on the surface of sulfur aluminate cement-based materials and found that the hydrophobic properties of methyl triethoxy silane had the optimal effect on carbonation resistance, effectively reducing porosity under 50 nm, and densifying the microscopic structure.

In addition to modifying the waterproofing, permeability, freeze−thaw damage, and other properties of cement-based materials, silane has been found by many researchers to decrease the mechanical properties of the modified cement-based materials to a certain extent.[20−23] As for repairing mortar, its mechanical properties are also important working properties. Therefore, it is urgent to develop new silane-modified materials that have little influence on the mechanical strength of concrete. Our research group uses isobutyltriethoxysilane (IBTS) as a monomer, uses GO to modify IBTS, and develops a new type of GO-IBTS composite emulsion. Research found that the GO-IBTS composite emulsion has improved compared with IBTS in terms of waterproof performance,[24−26] anti-icing performance,[27] anticarbonization performance,[28] antibacterial properties,[29] and chloride ion permeability,[28] and the protective mechanism is carefully analyzed. In addition, the test found that the mechanical properties of concrete mixed with GO-IBTS emulsion are stronger than those of IBTS. However, there is still a lack of internal mechanism explanation for the macroscopic phenomenon of GO-modified IBTS to improve the mechanical properties of concrete, and traditional experimental methods are difficult to break through the limitation of the nanometer scale. Therefore, the work uses molecular dynamics simulation to explore the mechanism at the atomic level.

Molecular dynamics simulation can visually display the information in microscopic physical and chemical processes, establish the relationship between nanoscale and macroscopic scale, and explore the internal mechanism to achieve the regulation of macroscopic performance. As an effective and powerful research tool, molecular dynamics simulation has been widely used in the field of concrete performance research. Hou et al.[30] explained the intrinsic mechanism of the mechanical properties of PEG, PVA, and PAA polymer fibers from the perspective of dynamics and energetics through molecular dynamics simulation. Wang et al.[31] studied the bonding properties of epoxy resin and the C−S−H interface under a corrosion environment and revealed the peeling mechanism of epoxy resin at the C−S−H interface. Zhou et al.[32] studied the effect of PVA fiber modification on the interface properties and revealed the interaction mechanism between the modified PVA fiber/nanosilica coating and the cementitious phase interface. In addition, molecular dynamics can reveal the microscopic physical and chemical processes and mechanisms of concrete under macroscopic phenomena such as erosion resistance,[33,34] elastic properties,[35−37] fluidity,[38] wettability,[39,40] fracture toughness,[41] etc.,[42] thus comprehensively understanding the structural properties and mechanical behavior of building materials and providing a strong guarantee for the prediction and modification of new materials.

Based on the reasons mentioned above, ettringite, the main hydration product of sulfoaluminate cement, is selected as the research base in this work, and molecular models of interfacial-bonding forces of IBTS/ettringite and GO-IBTS/ettringite are established through molecular dynamics simulation to reveal the sources of interfacial-bonding properties of IBTS, GO-IBTS, and ettringite from a molecular perspective. Additionally, the failure mechanism of the interface bond is studied to reveal the mechanism of GO modification of IBTS to improve its interface bond performance with ettringite and further understand the enhancement mechanism and approach of macroscopic mechanical properties to provide guiding significance for the subsequent modification of sulfoaluminate cement-based materials.

2. METHODS

2.1. Model Construction. The ideal initial unit cell of ettringite is shown in Figure 1a, which is established according to references.[43] Ettringite is a columnar structure with the molecular formula $3CaO{\cdot}Al_2O_3{\cdot}3CaSO_4{\cdot}32H_2O$. The $[Al(OH)_6]^{3-}$ octahedron and CaO_8 polyhedron distributed in the (001) direction are alternately arranged to form the basic unit of the cylinder $[Ca_3Al(OH)_612H_2O]^{3+}$, SO_4^{2-}, and the rest of the water molecules are distributed in the interspace of the cylinder in a hexagonal arrangement around the central axis of the positively charged cylinder.[44,45] The molecular structure of the modified waterproof material is shown in Figure 1b,c. Isobutyltriethoxysilane (IBTS) is selected for silane. Three ethoxy groups in IBTS will be hydrolyzed into silanol groups. As

https://doi.org/10.1021/acsomega.2c08123
ACS Omega 2023, 8, 16016−16031

shown in Figure 1b, the hydrolyzed IBTS is selected in the simulation. Subsequently, GO is used to modify the IBTS to improve its stability, and the changes in mechanical properties after modification are observed. The constructed GO sheet contains hydroxyl, epoxy, and carboxyl groups. The total coverage of the three surface functional groups is 20%, and the sheet size is about 24 Å × 20 Å. In the experiment, GO-modified silane is measured to improve its stability through dehydration reaction of the hydroxyl group of GO and hydroxyl group after hydrolysis of IBTS, which produced a bond.[24] Therefore, we construct the molecular model shown in Figure 1c, the GO-IBTS molecular model in which IBTS is connected to GO through a Si−O−C bond, and four IBTS are connected to each GO.

Based on the above unit model, the mechanical model with the structure as shown in Figure 2 is established. Based on the

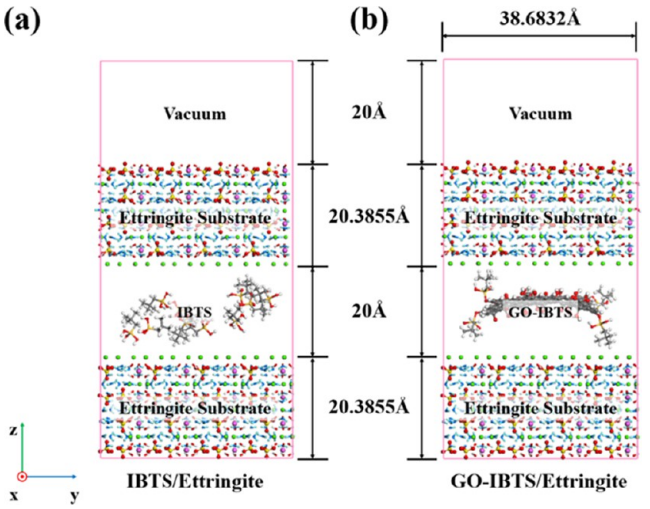

Figure 2. Mechanical model of (a) IBTS/ettringite and (b) GO-IBTS/ettringite.

ettringite unit cell, the supercell operation is carried out, and the middle 20 Å nanopore is reserved by translating the upper and lower substrates to place IBTS and GO-IBTS. The parameters of the upper and lower substrates are as follows: a = 44.6675 Å, b = 38.6832 Å, c = 20.3855 Å, α = 90°, β = 90°, and γ = 90°. The model is divided into the ettringite substrate and channels outside the interface with the surface calcium ions as the boundary. IBTS and GO-IBTS are randomly placed into the ettringite channels, and the number of IBTS is 10 to ensure that the relative molecular mass of the substances in the channels of the two systems is the same. To eliminate the statistical error caused by the size effect, a periodic boundary is set in the *xoy* plane during the simulation. To prevent the stretching phase from crossing the periodic boundary, a 20 Å vacuum layer is reserved above ettringite in the z direction.

2.2. Force Field and Simulation Details. The molecular force field is a potential function used to describe the interaction of the molecular system. In this simulation work, the empirical force field is used to describe the interaction of ettringite substrate, IBTS, and GO. Ettringite substrate adopts the ClayFF force field. The ClayFF[46] force field was developed by Cygan et al. It is mainly used to simulate inorganic materials such as oxides and hydroxides and has relatively mature applications. Meanwhile, the ClayFF force field has been widely used to simulate cement-based materials. The effect of silane and GO organic phases is described by the CVFF[47] force field, which is suitable for the calculation of various polypeptide proteins as well as a large number of organic molecules.

In this work, the whole system is simulated under LAMMPS,[48] and the steepest descent method is used to relax the whole system to minimize the energy of the whole system. The simulation process is divided into two stages. The first stage is the equilibrium stage. The established models of the two systems are subjected to free relaxation for 3 ns at a simulated temperature of 300 K in the NVT[49−51] ensemble, and the trajectories are output every 1 ps for subsequent interaction analysis. Figure 3 shows the force diagram of IBTS, GO-IBTS,

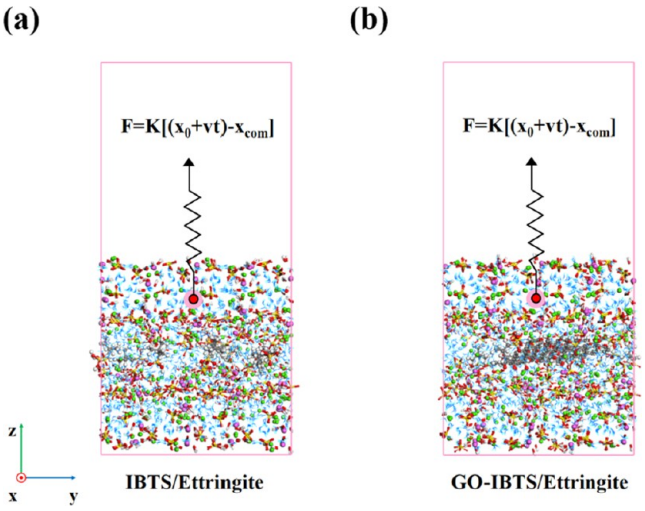

Figure 3. At 3000 ps, the equilibrium diagram and tensile force form of (a) IBTS/ettringite and (b) GO-IBTS/ettringite.

and ettringite substrate models. Under the NVT ensemble and 300 K simulation temperature, the external force in the form of the following formula is applied to the center of mass position of the upper substrate

$$F = K((X_0 + V \times t) - X_{com})$$

The external force applied is in the form of spring force, denoted by F.[52] K is the spring force constant. According to the verification of the simulation effect, 0.01 kcal/mol/nm^2 is the most appropriate value. X_0 is the coordinate in the Z direction of the center of mass applied by the external force. V is the tensile velocity of the external force along the Z-axis. We set 100, 80, 40, 10, 5, and 2 m/s to explore the influence of velocity on interface bonding. T is the simulation time. To ensure the same stretching distance under different stretching speeds, the simulation time is set as 0.2, 0.24, 0.5, 2, 4, and 10 ns, respectively. X_{com} is the dynamic position of the selected force acting on the ettringite center along the Z direction. Finally, the F and X_{com} data in the simulation process are extracted to obtain the pulling force−displacement curve.

3. RESULTS AND DISCUSSION

In this work, the molecular dynamics simulation method is used to study the changes in the bond properties of the whole system after adding IBTS and GO-IBTS to modify the ettringite system and to analyze the internal mechanism of GO-modified IBTS. The whole simulation is divided into two stages: the equilibrium adsorption stage and the dynamic tensile stage.

https://doi.org/10.1021/acsomega.2c08123
ACS Omega 2023, 8, 16016−16031

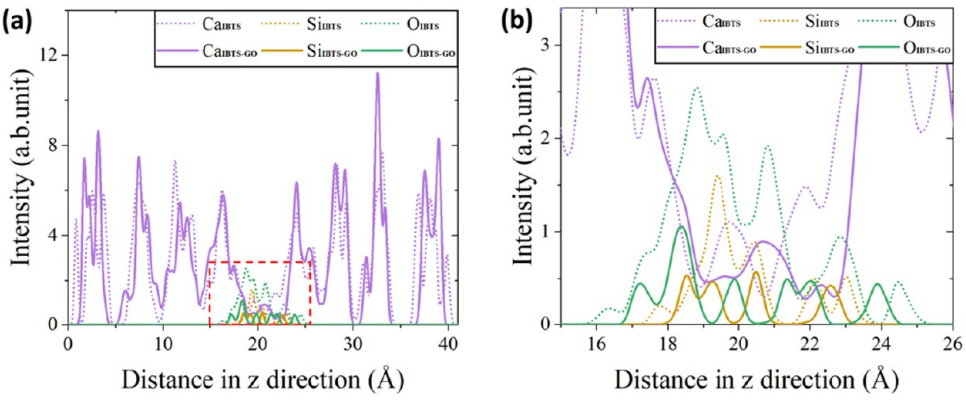

Figure 4. Density distribution of Ca, Si, and O atoms in (a) the IBTS system before and (b) after GO modification.

3.1. Equilibrium Adsorption Stage. The equilibrium adsorption stage takes the change of the centroid of the entire system as the judgment of the equilibrium of the simulated system, and both systems achieve equilibrium within 3000 ps. Through the local structure and dynamic characteristics of the two admixtures in the equilibrium stage, the interaction between them and ettringite is analyzed.

3.1.1. Molecular Structural Transformation of Ettringite. The atomic density distribution can directly show the distribution of the modified IBTS, GO-IBTS, and ettringite to obtain the binding characteristics of the interface structure between them. We extract the atomic density distribution of the IBTS system in the z direction before and after GO modification. In terms of atomic selection, the Ca atom is selected to represent the behavior characteristics of the substrate, and the Si atom and hydroxy O atom are selected to represent the behavior characteristics of IBTS. The atomic density distribution is shown in Figure 4, where the dashed line is the atomic density distribution before GO modification and the solid line is the atomic density distribution after GO modification. Each of the Ca ions in the upper and lower ettringite substrates around 20 Å on the abscissa of Figure 4a has four groups of intensity peaks, which represent the behavior characteristics of the four-layer ettringite in the established model. The four groups of intensity peaks show different distributions. The closer the IBTS is to 20 Å, the stronger the bias of Ca ion distribution and the more obvious the broadening. The peak width of Ca ions in the surface layer closest to IBTS at around 17 and 24 Å is the largest, and the density distribution of Ca, Si, and O atoms appears staggered in the red box. Figure 4b shows the enlarged figure, which qualitatively indicates that the Ca atomic layer in the basal surface layer interacts with IBTS.

By comparing the atomic density distribution curves before and after GO modification, it is found that the three atomic distributions of $Ca_{GO\text{-}IBTS}$, $Si_{GO\text{-}IBTS}$, and $O_{GO\text{-}IBTS}$ are more concentrated in the intermediate modified layer, indicating that the interaction between the intermediate modified layer and ettringite is enhanced by GO modification. Preliminary analysis of the reasons is as follows: (1) the connection of GO makes IBTS rely on the large specific surface area of GO, its degree of freedom has decreased, and the atomic distribution interval of $Si_{GO\text{-}IBTS}$ and $O_{IBTS\text{-}GO}$ has shrunk; (2) the hydroxyl, carboxyl, and epoxy oxygen functional groups on the surface of GO itself increase the interaction form between the intermediate modified layer and ettringite, making the $Ca_{GO\text{-}IBTS}$ curve biased to the intermediate modified layer distribution; and (3) the large specific surface area of GO is bonded to ettringite, which increases the stability of the ettringite to a certain extent and makes the intermediate modification more fully combined with ettringite.

The density distribution diagram in this section analyzes the molecular structure transformation of ettringite modified by IBTS and GO-IBTS from the atomic perspective. The bias distribution of the characteristic atomic curves qualitatively indicates that there is an interaction between IBTS, IBTS-GO, and ettringite. This section can guide the subsequent specific analysis of the forms of interaction, and the interaction range of 13−26 Å IBTS, GO-IBTS, and ettringite determined by the atomic distribution diagram can be used to define the scope of subsequent radial distribution curve analysis and increase the accuracy of data analysis.

3.1.2. Interface Ca−O Bond and Its Structure. The radial distribution function can reflect the order degree of the structure.[39] By analyzing the sharpness, width, and position of the peak of RDF, the spatial correlation between ions and ions, ions and solid atoms, and water molecules and solid atoms can be qualitatively obtained. Figure 5 shows the RDF and local structure diagrams of calcium atoms on the surface layer of ettringite substrate and oxygen atoms on the functional group of IBTS before and after GO modification of the IBTS system. Among them, the limitation of the data analysis range of the radial distribution curve in this section is taken from 13 to 26 Å obtained by the atomic density distribution curve of the previous section. In the RDF curve of Figure 5a, the dashed line is the pure IBTS system before GO modification and the solid line is the GO-IBTS system after GO modification.

In the IBTS curve, it can be seen that the $Ca-O_{IBTS}$ curve has the first peak at 2.65 Å, and this bond length is within the range of 2.35−2.75 Å in the ettringite crystal, indicating that the added IBTS can produce a strong interionic interaction with the Ca ion of the ettringite substrate through the oxygen atom of the alcohol hydroxyl group. The Ca−O ion pair is formed, and its structure is shown in Figure 5b. In addition, the $Ca-O_{IBTS}$ curve has a second peak at 3.95−4.55 Å, which is beyond the Ca−O bond range, indicating that there is a remote interaction between Ca and O atoms. The local structure (Figure 5c) is extracted to observe the action form, and it is found that the hydroxyl oxygen atom of IBTS had an indirect interaction with the Ca atom through forming a hydrogen bond bridge interaction with the water molecule, and the specific expression form is "$Ca-Ow-Hw-O_{IBTS}$". The above two direct and indirect forms of interaction realize the bond between IBTS and ettringite.

The GO-IBTS curve after IBTS is modified by GO has the first sharp peak at 2.55 Å and the second broad peak at 3.95 Å.

https://doi.org/10.1021/acsomega.2c08123
ACS Omega 2023, 8, 16016−16031

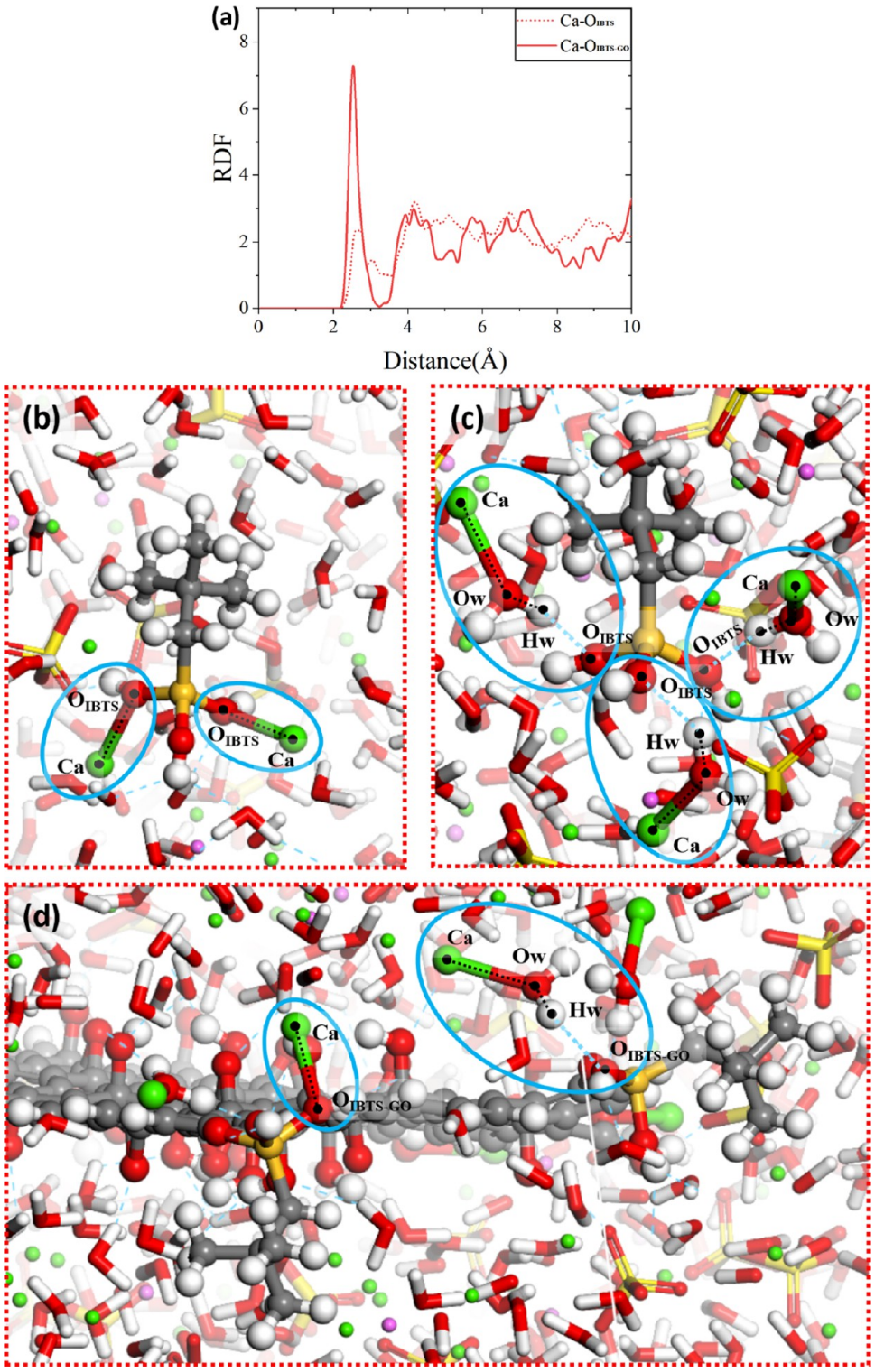

Figure 5. (a) Radial distribution function diagram; local structure diagram of (b, c) Ca−O bond of IBTS before and (d) after GO modification.

We extract the local structure (Figure 5d) and find that there are also two forms of interaction between IBTS and Ca ions of the ettringite substrate: (1) the left side of Figure 5d shows the direct effect of the Ca−O ionic bond. (2) The right side of Figure 5d shows the indirect effect of "Ca−Ow−Hw−$O_{GO\text{-}IBTS}$" remotely. Comparing the two solid and dashed line curves, it is found that the modification of GO reduces the two peak positions of RDF and the sharpness of the first peak increases significantly. This phenomenon indicates that the GO connection effectively enhances the interaction between IBTS and ettringite substrate without changing the interaction form between them. This effect is closely related to the large surface area of GO, which effectively limits the confusion of the upper and lower ettringite, makes Ca ions accumulate on the GO surface, limits the degree of freedom of Ca ions, and increases the probability and strength of interaction between GO-linked IBTS and Ca. In addition, functional groups carried by GO will

https://doi.org/10.1021/acsomega.2c08123
ACS Omega 2023, 8, 16016−16031

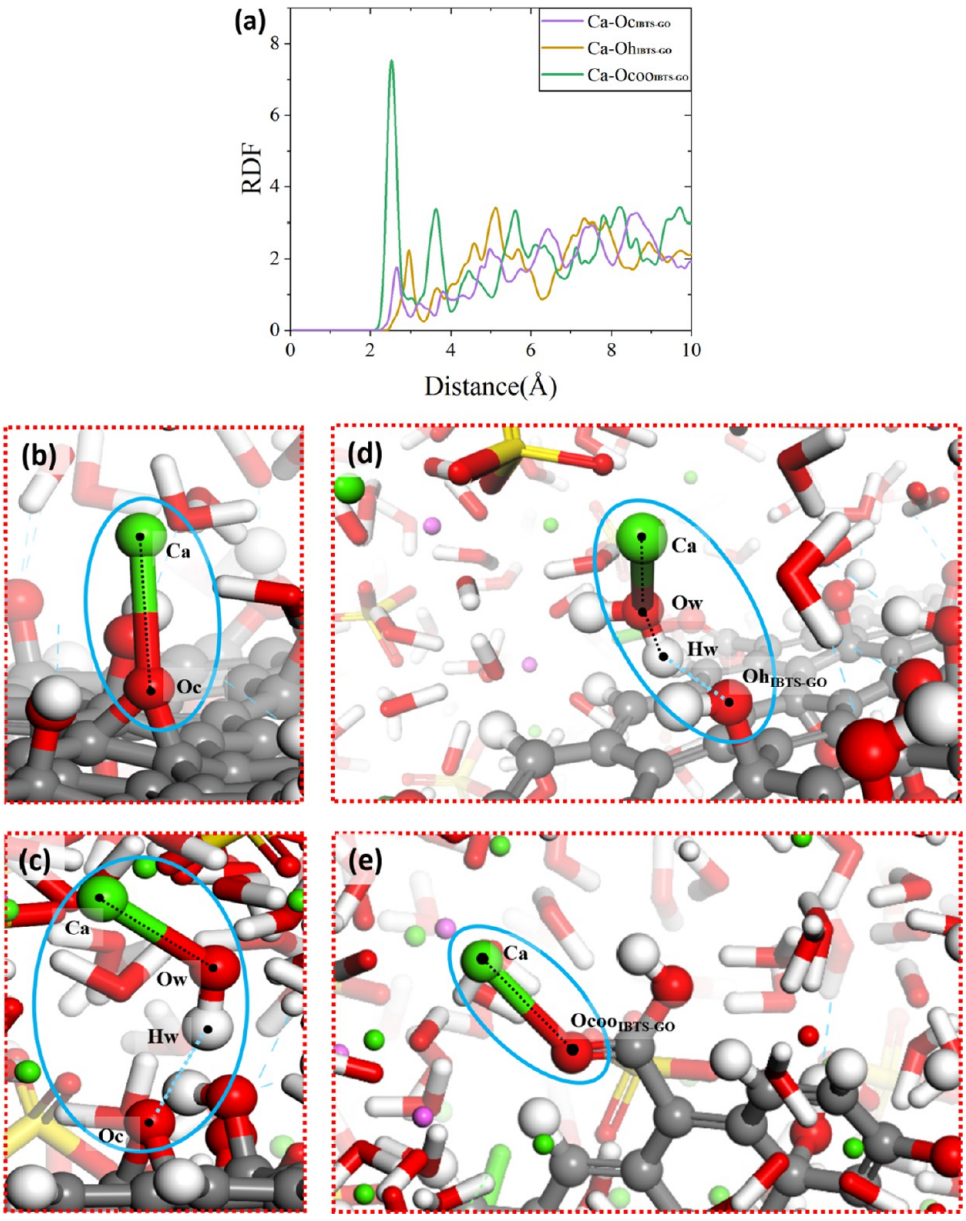

Figure 6. (a) Radial distribution function of the GO-IBTS system and (b−e) local structure diagram of the Ca−O ionic bond in GO.

also interact with Ca ions, thus attracting Ca ions to gather near GO. This interaction will be analyzed below.

In addition to modifying the interaction of the interface of IBTS and ettringite, GO also interacts with the ettringite substrate to affect the bonding property of the system. Figure 6 shows the RDF curves and local structure diagrams of GO surface functional groups and ettringite surface Ca ions in the GO-IBTS system. It can be observed from the RDF curve in Figure 6a that Ca−Oc$_{GO-IBTS}$, Ca−Oh$_{GO-IBTS}$, and Ca−Ocoo$_{GO-IBTS}$ have the first peak at 2.65, 2.95, and 2.55 Å, respectively, indicating that the epoxy, hydroxyl, and carboxyl groups on GO have different degrees of ionic interaction with the Ca atoms of ettringite. The smaller the peak position, the stronger the ion interaction is. Therefore, the curve shows that the ionic interaction size of the three functional groups of GO is carboxyl group > epoxy group > hydroxyl group.

The specific bond forms of three functional groups are observed separately. First, the peak position of the first peak of Ca−Oc$_{GO-IBTS}$ is at 2.65 Å, indicating that Ca forms a direct ionic bond cooperation with O, and the local structure is shown in Figure 6b. The curve of Ca−Oc$_{GO-IBTS}$ has a broad second peak at 3.25 Å, which reflects the indirect interaction between Ca−Oc as shown in Figure 6c. The Ca ion binds to the surrounding water molecules, and the H atom in the hydroxyl group of water molecules forms a hydrogen bond interaction with the Oc atom; thus, the Ca ions have a remote interaction with the Oc atoms. Compared with the first peak of Ca−Oc$_{GO-IBTS}$, the first peak of the RDF curve of Ca−Oh$_{GO-IBTS}$ shifts to the right. The peak at 2.95 Å shows that the bond form of Ca and Oc is indirect. As shown in Figure 6d, the Ca ions bind to the surrounding water molecules. The H atom of the hydroxyl group forms a hydrogen bond with the Oh atom to realize the remote and indirect capture of the Ca ion by Oh. Compared with the previous two curves, the first peak of Ca−Ocoo$_{GO-IBTS}$ is sharper and smaller, indicating that there is a strong interaction between the Ca atoms in the surface layer of ettringite and the carboxyl group of GO. And Ocoo has a stronger ability to directly capture Ca ions in the short range than Oc, forming Ca−O ion pairs on the left of

https://doi.org/10.1021/acsomega.2c08123
ACS Omega 2023, 8, 16016−16031

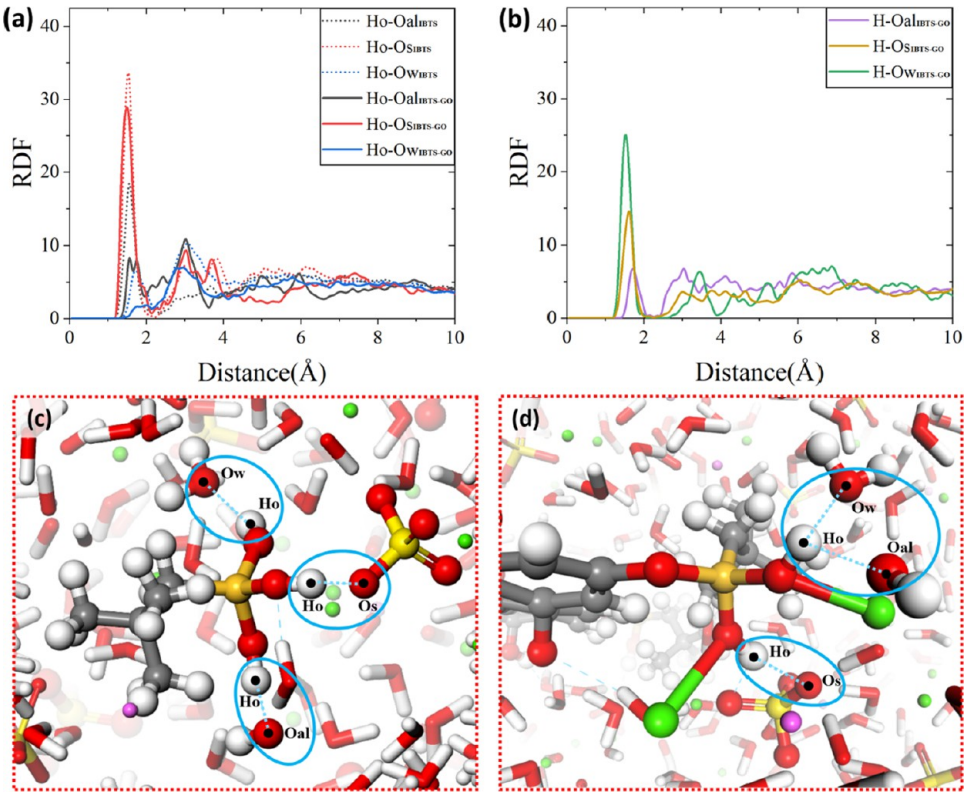

Figure 7. Radial distribution function of hydrogen bonds of (a) IBTS before and (b) after GO modification; local structure diagram of (c) IBTS before and (d) after GO modification.

Figure 6e. Its second peak is located at 3.65 Å, indicating that Ocoo also has an indirect effect on the Ca ions in the form of Ca−Ow−Hw−Oh. The local structure is shown on the right of Figure 6e.

3.1.3. Hydrogen Bond Network. In addition to Ca−O ion interactions, hydrogen bond networks formed between water molecules, aluminum hydroxyl groups, sulfate, and functional groups also play a pivotal role in the bonding properties between IBTS, GO, and ettringite substrate. Figure 7 shows the RDF curves and local structure diagram of the hydrogen bonds formed between IBTS and ettringite before and after GO modification. In the RDF graph of Figure 7a, the solid lines are those of the IBTS system, and the dashed lines are those of the GO-IBTS system. All curves in the figure satisfy the hydrogen bond formation condition that the distance between hydrogen donor and oxygen acceptor should be less than 2.45 Å. Hydroxyl hydrogen atoms of IBTS, as donors, can form three types of hydrogen bonds with aluminum hydroxyl groups of ettringite substrate, sulfate, and oxygen acceptors of water molecules.

It can be observed from the curve that these three types of hydrogen bonds exhibit different degrees of interaction. The peak positions of Ho−Oal, Ho−Os, and Ho−Ow of the dashed IBTS curves are 1.55, 1.55, and 1.75 Å, respectively. The relationship between the hydrogen bond interaction of the three is as follows: Ho−Os > Ho−Oal > Ho−Ow, and the diagram of the bonding mode is shown in Figure 7c. The solid line after GO modification of IBTS shows that the GO connection does not change the peak positions of the three hydrogen bonds but decreases the peak values. This is because the hydroxyl group of GO is connected to the hydroxyl group of IBTS through a dehydration reaction, and the reduction of the hydroxyl site of IBTS decreases the peak value of three types of hydrogen bonds. The schematic diagram of the hydrogen bond structure of IBTS after GO modification is shown in Figure 7d.

Similarly, GO would form hydrogen bond interactions with the ettringite substrate to enhance the stability of the interface. As donors, hydrogen atoms of GO functional groups can form three types of hydrogen bonds with the aluminum hydroxyl group of ettringite substrate, sulfate group, and oxygen acceptor of the water molecule, as shown in Figure 7b. Besides, the RDF curve of IBTS forming hydrogen bonds with water molecules of ettringite substrate has been noted and the second peak is larger than the first peak, indicating that the hydrogen bond interaction between IBTS and ettringite substrate is mainly derived from the hydrogen bond network formed by indirect interaction.

3.1.4. Time Correlation Function. It is qualitatively obtained from the previous local structure analysis that ionic bonds and hydrogen bonds between calcium atoms and oxygen in IBTS and GO functional groups play a pivotal role in improving the bonding properties between IBTS and ettringite. Time correlation function (TCF)[52,53] can quantitatively describe the strength and stability of various chemical bonds formed between molecules, between ions, and between ions and molecules. The relationship is shown as follows

$$C(t) = \frac{\langle \delta b(t)\ \delta b(0) \rangle}{\langle \delta b(0)\ \delta b(0) \rangle}$$

where $b(t)$ is a binary operator, which only changes with the change of time, and its value is only 0 or 1. The value is 1 if bonds are formed between atoms, 0 otherwise, and $\langle b \rangle$ is the average of b. The chemical bonds in the system will form or break over time. The TCF value of the two atoms is close to 1, indicating that the bond between them is stable. On the contrary, if the

https://doi.org/10.1021/acsomega.2c08123
ACS Omega 2023, 8, 16016−16031

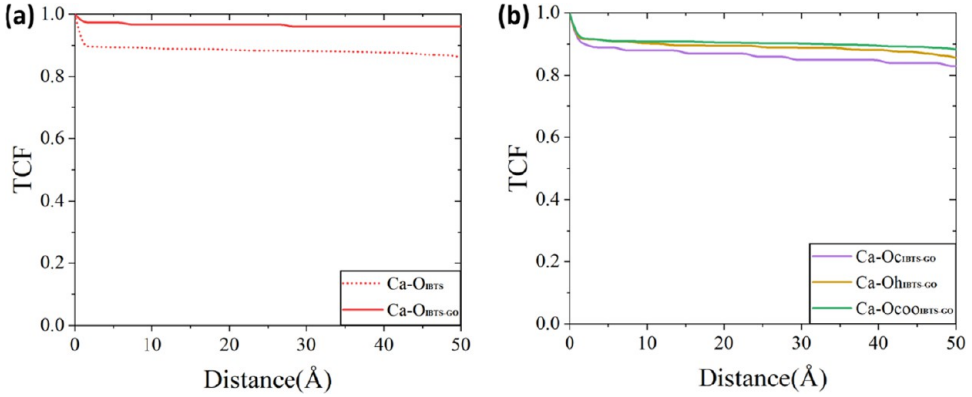

Figure 8. TCF of the Ca−O ionic bond: (a) ionic bonds of IBTS before and after GO modification and (b) ionic bond of GO.

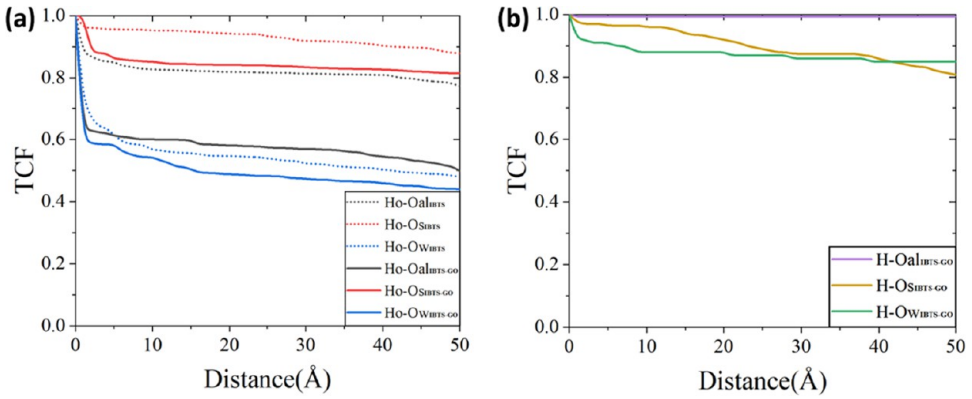

Figure 9. TCF of hydrogen bonds: (a) hydrogen bonds of IBTS before and after GO modification and (b) hydrogen bonds of GO.

bond stability is poor, the value of TCF will quickly decay to 0 with the increase of time.

Figure 8 shows the TCF of the Ca−O ionic bond at the modified interface, where Figure 8a shows the stability of the Ca−O ionic bond formed by the hydroxyl oxygen atom of IBTS and Ca ions before and after GO modification, and the dashed line is the GO-unmodified system. The solid line shows the GO-modified system, and Figure 8b shows the stability of the Ca−O ionic bond formed between the three oxygen atoms on the GO functional group and Ca ions. It can be seen from Figure 8a that the TCF values of Ca−O_{IBTS} and Ca−$O_{GO\text{-}IBTS}$ in the two systems show a small attenuation. At 50 ps, values of Ca−O_{IBTS} and Ca−$O_{GO\text{-}IBTS}$ decay to 0.86 and 0.96, respectively, which indicates that the hydroxyl oxygen atom of IBTS can form a relatively stable ionic bond with Ca of ettringite, and the modification of GO increases the stability of the Ca−O bond between IBTS and ettringite. Three kinds of Ca−O ionic bonds in Figure 8b, Ca−$Oc_{GO\text{-}IBTS}$, Ca−$Oh_{GO\text{-}IBTS}$, and Ca−$Ocoo_{GO\text{-}IBTS}$, formed by the oxygen-containing functional groups of epoxy, hydroxyl, and carboxyl groups on the surface of GO and Ca, show different stabilities. At 50 ps, values of Ca−$Oc_{GO\text{-}IBTS}$, Ca−$Oh_{GO\text{-}IBTS}$, and Ca−$Ocoo_{GO\text{-}IBTS}$ decay to 0.83, 0.86, and 0.88, respectively. The hydroxyl oxygen atom of GO has high electronegativity and a strong affinity with Ca ions to make the Ca−Oh with high stability. Compared with Oh, the Ocoo of GO is more electronegative, Ca ions show a stronger affinity for carboxyl groups, and the Ca−Ocoo bond has higher stability. At the same time, combined with the local structure analysis, the two oxygen atoms of the carboxyl group enhance the stability of the ion connection. Based on the above TCF analysis, the order of bond stability between calcium ions and different functional groups is as follows: Ca−$Ocoo_{GO\text{-}IBTS}$ > Ca−$Oh_{GO\text{-}IBTS}$ > Ca−$Oc_{GO\text{-}IBTS}$.

Figure 9 shows the TCF diagram of the hydrogen bond, where Figure 9a shows the stability of the hydrogen bond formed between the hydroxyl hydrogen atom of IBTS and oxygen of the ettringite substrate before and after GO modification; the dashed line is the GO-unmodified system, and the solid line is the GO-modified system. Figure 9b shows the stability of the hydrogen atom of the GO functional group forming a hydrogen bond with oxygen atoms of the ettringite substrate. The TCF curve in Figure 9a shows that the three hydrogen bonds formed by the substrate exhibit different stabilities. This TCF value at 50 ps shows that Ho−Os, HO−Oal, and Ho−Ow decreased to 0.88, 0.78, and 0.48, respectively, indicating that the stability order of the three hydrogen bonds is Ho−Os > Ho−Oal > Ho−Ow. This also indicates that the hydrogen bond between IBTS and ettringite mainly originates from the oxygen atom in the aluminum hydroxyl group or sulfate. According to the RDF analysis above, the hydrogen bond interaction between IBTS and water molecules mainly comes from the indirect hydrogen bond network, which is relatively poor in stability, and it can well explain the reason the TCF value of Ho−Ow decreases by half. After the GO modification, the TCF values of the hydrogen bond formed by IBTS and ettringite decrease, Ho−Os decreases by 7%, Ho−Oal decreases by 36%, and Ho−Ow decreases by 8%, which shows that the modification of GO can reduce the stability of the IBTS hydrogen bond. The modification of GO reduces the number of hydroxyl groups in IBTS, thus affecting the bonding of hydrogen bonds. In addition, the competitive relationship between the functional groups of GO and IBTS will

https://doi.org/10.1021/acsomega.2c08123
ACS Omega 2023, 8, 16016−16031

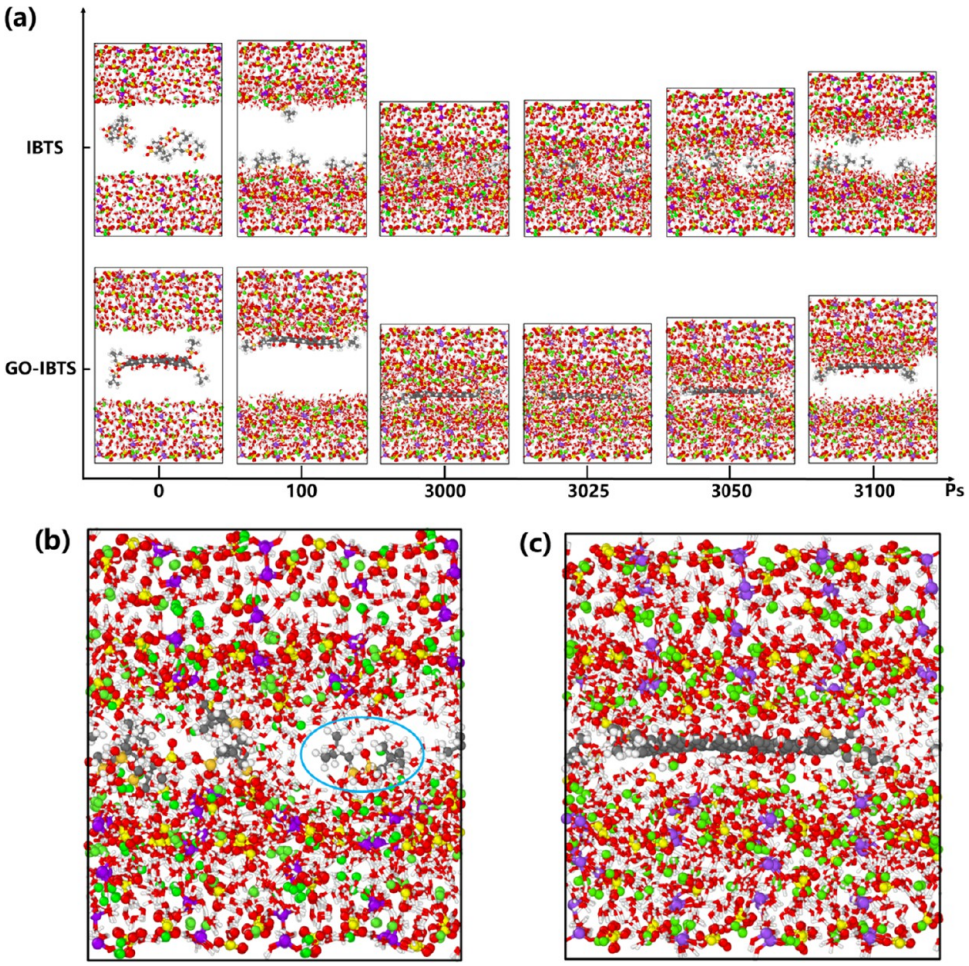

Figure 10. (a) Structure diagram of IBTS, GO-IBTS, and ettringite at different simulation times; (b) at 3050 ps, the structure diagram of IBTS; and (c) at 3050 ps, the structure diagram of GO-IBTS.

preoccupy the binding sites, affecting the stability of forming hydrogen bonds between IBTS and the ettringite substrate.

Figure 9b shows the TCF curve of GO-forming hydrogen bonds. It can be found that the stability of GO-forming hydrogen bonds with aluminum hydroxyl groups is basically unchanged, indicating that GO can form stable hydrogen bonds with aluminum hydroxyl groups. H−$Os_{GO\text{-}IBTS}$ and H−$Ow_{GO\text{-}IBTS}$ decrease to 0.81 and 0.85, respectively. By comparison, the hydrogen bond stability of GO is significantly stronger than that of IBTS. Therefore, it can be said that the stability of the hydrogen bond formed by ettringite is improved by the modification of GO, which enhances the interface-bonding property between ettringite and modified substances.

3.2. Dynamic Tensile Stage. Based on the analysis of the interaction forms and stability between IBTS, GO-IBTS, and ettringite in the previous equilibrium stage, this section mainly investigates the strength of bond properties between them and the reasons for bond failure in the dynamic tensile simulation stage.

3.2.1. Tensile Simulation Diagram. To reduce the influence of simulation velocity on tensile behavior, we select the minimum tensile velocity of 2 m/s as an example and extract the structure diagram of the tensile phase to intuitively display its behavior characteristics. Figure 10a shows the behavior diagrams of IBTS, GO-IBTS, and ettringite at different moments in the whole simulation process. It can be observed from Figure 10 that IBTS and GO-IBTS are unilaterally adsorbed due to the electronegative attraction of ettringite in the equilibrium stage from 0 to 100 ps, resulting in bonding. Then, the two substrates gradually converge and come to bond with each other from 100 to 3000 ps. After 3000 ps, the tensile force is gradually applied, and at 3025 ps, the volume of the IBTS system first shows tensile growth. At 3050 ps, the IBTS of the middle layer shows obvious peeling voids, and GO-IBTS bonded closely, which qualitatively indicates that GO-IBTS is stronger than IBTS. After 3100 ps, IBTS, GO-IBTS, and ettringite have an obvious interface peeling and only adsorb on one side of the substrate.

At 3050 ps, Figure 10b shows that the behavior of IBTS at the interface during the stretching stage is consistent: the hydrophilic hydroxyl end of IBTS tends to the ettringite distribution on the proximal side, while the hydrophobic alkyl end tends to the middle plane distribution. As can be seen from the molecular behavior diagram, the fracture surface in the tensile stage occurs at the interface between IBTS and ettringite. The difference between the hydrophilicity and hydrophobicity of both ends of IBTS leads to the bonding between IBTS and ettringite only on one side, which becomes the weak link of interface tensile fracture. At the same time, this phenomenon is consistent with previous studies on the hydrophobicity of IBTS: the hydrophilic end of IBTS interacts with ettringite, and the hydrophobic endpoints into the channel, thus protecting IBTS from water transport in the ettringite channel. Figure 10c of the GO-IBTS-

https://doi.org/10.1021/acsomega.2c08123
ACS Omega 2023, 8, 16016−16031

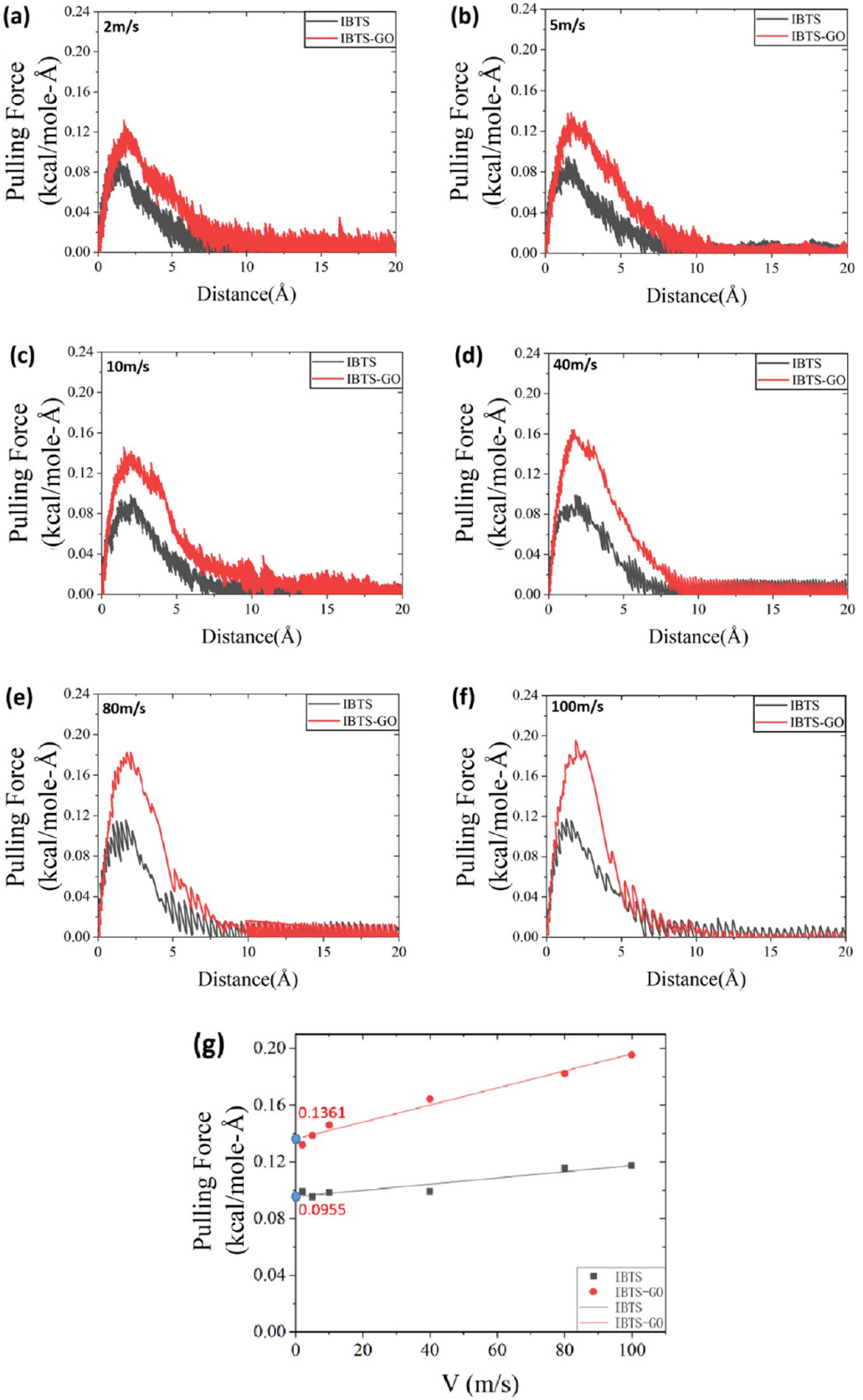

Figure 11. Tensile curves of IBTS and GO-IBTS at tensile speeds of (a) 2 m/s, (b) 5 m/s, (c) 10 m/s, (d) 40 m/s, (e) 80 m/s, and (f) 100 m/s; (g) the fitted force−velocity curve.

modified ettringite system at 3050 ps shows that the functional groups on the surface of GO itself have two sides, which can realize the interaction with ettringite on both sides. Moreover, the large specific area of GO makes it have higher cohesion and

https://doi.org/10.1021/acsomega.2c08123
ACS Omega 2023, 8, 16016−16031

bind more closely with ettringite. IBTS is connected with GO by the hydroxyl group, which makes them have a synergistic effect. IBTS improves its adhesion by relying on the strong interaction between GO and ettringite to realize the improvement of the ettringite bond performance of the IBTS-GO-modified system.

In addition, this work well explains the rationality of the waterproof modification of ettringite by GO-IBTS. The bond performance between GO and ettringite is better than that of IBTS. GO can capture the IBTS that are removed from ettringite adsorption due to water transfer, realizing the stability modification of IBTS by GO, to achieve a better waterproof effect.

3.2.2. Tensile Curve. On the basis of qualitative analysis of the molecular structure diagram above, we extract the mechanical curve at the tensile speed for quantitative analysis, as shown in Figure 1111a−f. The tensile curves at different speeds show the following phenomena: (1) the whole tensile curve is divided into two stages. In the former stage, the curve increases with the increase of tensile displacement. In this stage, the tensile force needs to overcome the bonding between IBTS, GO-IBTS, and ettringite substrate, and the tensile force increases gradually. When the tensile force reaches the maximum, that is, the top part of the curve, the tensile force has completely overcome the bonding force between the two, and IBTS, GO-IBTS, and ettringite substrate are separated. Then, the curve enters the unloading stage, and the separated upper ettringite substrate part breaks away from the bonding effect and is pulled up by gradually small forces. (2) The stripping tensile force of the GO-IBTS system is higher than that of the IBTS system. The mechanical curves of six groups at different speeds all show that the tensile force required for the separation of GO-IBTS and ettringite substrate to overcome the bonding effect is greater than that of IBTS, indicating that the modification of GO can effectively improve the interface-bonding property between IBTS and ettringite substrate. (3) The tensile speed affects the force required for interface peeling. By comparing the required peeling tensile force at different speeds, it is found that with the increase of the tensile speed, the required peeling force increases gradually in both systems. In addition, with the increase of the tensile speed, the degree to which GO modification improves the tensile force of IBTS gradually increases. As shown in Table 1, the tensile force improvement degree increased from 33.22%

Table 1. Size of Interface Pulling Force and the Degree of GO Modification Enhancement at Different Speeds

tensile speed (m/s)	pulling force of IBTS separation (kcal/mol-Å)	pulling force of GO-IBTS separation (kcal/mol-Å)	lift degree of GO separation pulling force (%)
2	0.09902	0.13191	33.22
5	0.09527	0.13857	45.45
10	0.09853	0.146	48.18
40	0.09917	0.16429	65.67
80	0.11543	0.18233	57.96
100	0.11744	0.19532	66.31

at 2 m/s to 66.31% at 100 m/s. It can be seen that the tensile speed will have a certain influence on the size of the peeling force, which is consistent with the actual macroscopic mechanic's test.

Therefore, in this work, the stretching rate and tensile force are curve-fitted, as shown in Figure 11g. The tensile force whose theoretical tensile rate is 0 is found by fitting the curve, and the influence of the tensile rate on the simulation results is eliminated. As can be seen from Figure 11g, when the speed is 0, the tensile force of IBTS is 0.0955 kcal/mol-Å and that of GO-IBTS is 0.1361 kcal/mol-Å. The modification of GO makes the tensile force of GO-IBTS increase by 42.51% compared with that of IBTS, which greatly enhances the bonding property of the interface.

3.2.3. Dynamic Coordination Number. According to the interface analysis in the equilibrium stage, IBTS and GO-IBTS interact with ettringite through the Ca−O ionic bond and hydrogen bond, thus realizing the interface adhesion between them. Starting from the source of bond properties, this work analyzes the dynamic changes in the number of bonds formed by the two types of bonds before and after interface peeling to reveal the causes of the interface tensile failure process and the reasons for the improvement of bond properties by GO modification of IBTS from the perspective of bond bonding.

Figure 12 shows the dynamic coordination number of the whole simulation process. The first 3000 ps is the equilibrium adsorption state and the last 200 ps is the tensile stage. Figure 12a shows the coordination situation of Ca−O ionic bonds formed by IBTS before and after GO modification, which is analyzed in combination with the previous local structure diagram. At the initial stage of 0−100 ps, the number of Ca−O ion bond coordination number of IBTS and GO-IBTS systems increases sharply, indicating that IBTS and the ettringite substrate have strong interaction through the Ca−O ion bond, which makes IBTS adsorbed on the unilateral ettringite substrate. 100−3000 ps is the equilibrium adsorption stage. After adsorbing IBTS and GO-IBTS, the upper and lower layers of ettringite substrates have a strong adsorption effect due to the difference in electronegativity, which makes the two substrates converge and realize the balance of the whole system. It can be found from the curve that the dynamic coordination number fluctuation of the Ca−O bond of IBTS is greater than that of the GO-IBTS system during the equilibrium process, indicating that the Ca−O ionic bond of IBTS is prone to bond breakage and recombination and has poor stability, which is consistent with the previous TCF analysis results.

It is worth noting that in the equilibrium stage, both curves have a period of the first decline and then stability, which are 2700−3000 ps of IBTS and 1000−3000 ps of GO-IBTS, respectively. Combined with the local analysis figure, it can be seen that the curve process of 2700−2900 ps of IBTS and 1000−1300 ps of GO-IBTS corresponds to the stage of complete adsorption and bonding of the two substrates, and the interface bonding of the Ca−O bond is weakened by the coupling effect of the bonding of the two substrates: the number of bonds formed by IBTS of the two systems shows a downward trend. Figure 12c,d shows the density contour map of Ca ions and IBTS hydroxyl oxygen atoms during the complete bonding stage of the two substrates. The red is the hydroxyl oxygen atom representing the behavior of IBTS, and the green is the calcium atom of the base. Figure 12c shows that most of the oxygen atom trajectories are scattered, indicating that the Ca−O bond stability is poor. Figure 12d shows that the link of GO makes the oxygen atom trajectories of IBTS more concentrated, indicating that the modification of GO increases the stability of ionic bonds of IBTS. In addition, as can be seen from the density contour map of GO and basal calcium atoms in Figure 12e, the trajectories of GO are more concentrated and the ionic bonds formed by GO are more stable, which is closely related to its large specific surface area. The time of 2900−3000 ps of IBTS and 1600−3000 ps of GO-IBTS corresponds to the stage after

https://doi.org/10.1021/acsomega.2c08123
ACS Omega 2023, 8, 16016−16031

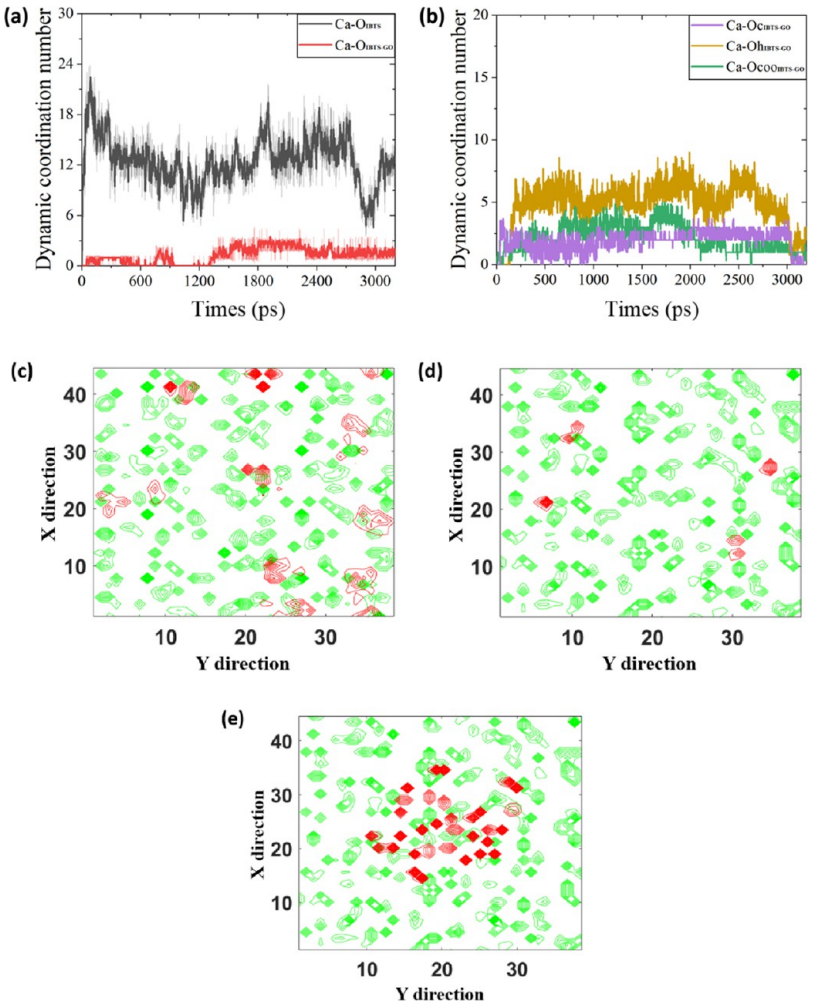

Figure 12. (a) Ca−O dynamic coordination number of IBTS before and after GO modification; (b) GO-IBTS system, the Ca−O dynamic coordination number of IBTS; (c) trajectories of oxygen atoms of IBTS and calcium atoms of ettringite in the IBTS system; (d) trajectories of oxygen atoms of IBTS and calcium atoms of ettringite in the GO/IBTS system; and (e) trajectories of oxygen atoms of GO and calcium atoms of ettringite in the GO/IBTS system.

the stable bonding of the two substrates. The number of Ca−O bonds of IBTS at the interface of the two systems shows a stable value, and the stability of the bonds is increased.

During the tensile stage of 3000−3200 ps, the number of Ca−O bonds of IBTS shows an increasing trend, indicating that with the gradual separation of the two substrates during the stretch, IBTS gradually gets rid of the influence of the nonadsorbed ettringite substrate on the bonding of the IBTS-adsorbed ettringite, showing the Ca−O ionic bond properties formed by the unilateral adsorption of ettringite on IBTS. This process can be regarded as the reverse process of the adsorption and converging of the 2700−2900 ps two substrates of IBTS. Compared with the tensile stage of IBTS, the number of ionic bonds formed by IBTS does not fluctuate significantly, indicating that the modification of GO makes the binding of IBTS to the Ca−O ionic bonds of ettringite on the adsorption side more stable and is not affected by the nonadsorption ettringite substrate.

In addition to the effect of GO modification on the bond number of IBTS, the bond number of its own functional groups with ettringite is shown in Figure 12b. Similarly, after the initial stage of unilateral adsorption of GO-IBTS and ettringite, the number of three kinds of Ca−O bonds of GO increased. The coordination number curve is stable after the two substrates are attracted to each other and reach the equilibrium stage. At the last stretch stage of 3000−3200 ps, the three Ca−O bonds all show a significant decrease, indicating that the interface stretch makes the Ca−O bond between GO and ettringite break, which leads to the failure of interface bonding. In addition, the number of coordination numbers after complete tensile separation can be found to be significantly decreased compared with that in the equilibrium adsorption stage, indicating that compared with IBTS, GO can increase the bonding property between the two substrates in the equilibrium adsorption stage by relying on its double-sided functional group characteristics.

In addition to the Ca−O ionic bond, hydrogen bonding is also the source of interfacial bonding. Therefore, in the interfacial tensile fracture stage, in addition to the coordination number of the Ca−O ion bond, the relationship between the hydrogen bond and interfacial bond failure is analyzed. Figure 13 shows the dynamic coordination numbers of IBTS and GO-IBTS systems, where Figure 13a,b shows the coordination numbers of hydrogen bonds formed between IBTS and ettringite substrate under the two systems. Similar to the case of the Ca−O ionic bond, the number of hydrogen bond coordination in IBTS and GO-IBTS systems first increased after the initial one-sided

https://doi.org/10.1021/acsomega.2c08123
ACS Omega 2023, 8, 16016−16031

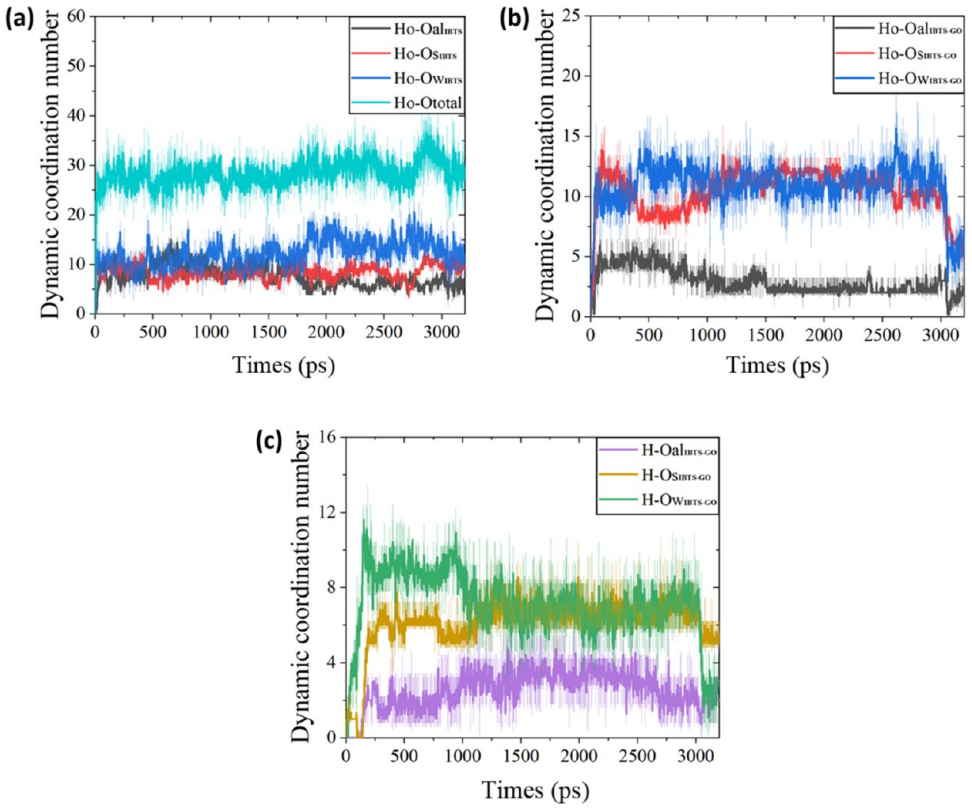

Figure 13. Dynamic coordination number: (a) IBTS system, the number of hydrogen bonds of IBTS; (b) GO-IBTS system, the number of hydrogen bonds of IBTS; and (c) GO-IBTS system, the number of hydrogen bonds of GO.

adsorption process. The coordination number of the three hydrogen bonds of IBTS shows different changes. From 2700 to 2900 ps, the coordination number of Ho−Oal$_{IBTS}$ and Ho−Os$_{IBTS}$ increases, while the coordination number of Ho−Ow decreases. The results indicate that the number of hydrogen bonds formed by IBTS with the ettringite aluminum hydroxyl group and sulfate group increases, while the number of hydrogen bonds formed by IBTS with water molecules decreases, which is closely related to the degree of freedom of the three substrate substances. Compared with water molecules, the aluminum hydroxyl group and sulfate group have poor degrees of freedom. In the phase of substrate approaching, the aluminum hydroxyl group and sulfate group increase the possibility of forming hydrogen bonds with bilateral substrates, increasing in coordination number. However, because of the free distribution of water molecules in ettringite, the coordination number of water molecules tends to decrease as ettringite comes closer together and exhibits large mobility. In general, it can be seen from the Ho−O total curve that the total number of hydrogen bonds still shows an upward trend in the base convergence stage. At the same time, limited by the large specific surface area of GO, the degrees of freedom of IBTS in the GO-IBTS system decreased, so the coordination number did not change significantly in the phase of substrate convergence.

Figure 13a,b in the mechanical tensile stage of 3000−3200 ps shows that the number of hydrogen bonds in IBTS and GO-IBTS systems decreased, and Figure 13c shows the number of hydrogen bonds between GO and ettringite in the GO-IBTS system. Three types of hydrogen bonds formed between GO and ettringite substrate also showed a significant decrease during the stretch phase. The three figures show that the rupture of hydrogen bonds at the interface caused by tension is also one of the reasons for the failure of interface-bonding properties.

3.2.4. Interaction Energy. In addition to analyzing the reasons for the failure of interface-bonding properties in the tensile stage from the perspective of interface bonding in the previous section, this section analyzes the failure from the perspective of interaction energy. We extract the interaction energy curves of IBTS, GO-IBTS, and ettringite interface at the stretch stage of 3000−3200 ps, as shown in Figure 14. It can be seen from the curve that at 3000 ps equilibrium adsorption stage, the interaction energy between IBTS and ettringite interface is −490 kcal/mol, while that of GO-IBTS is −650 kcal/mol. The interaction energy of IBTS is higher than that of GO-IBTS, indicating that the modification of GO reduces the interaction energy between IBTS and ettringite interface. As a result, the

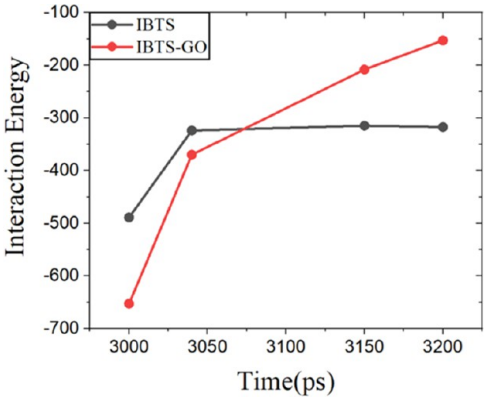

Figure 14. Interaction energy curve.

https://doi.org/10.1021/acsomega.2c08123
ACS Omega 2023, 8, 16016−16031

interface adhesion performance of GO-IBTS and ettringite is stronger than that of IBTS, and the interface bonding is more stable. At 3050 ps, the interface of IBTS, GO-IBTS, and ettringite breaks away due to the effect of tensile force, and the interface interaction energy of the two systems increases, showing the adsorption characteristics of IBTS, GO-IBTS, and unilateral ettringite substrate. The energy order of the two at the initial separation stage of 3050 ps is $E_{IBTS} > E_{GO\text{-}IBTS}$.

In the interface separation process of 3000−3050 ps, the relationship between the interaction energy change of the two systems is $E_{IBTS} < E_{GO\text{-}IBTS}$. It indicates that the tensile force makes GO-IBTS and ettringite from a stable binding state to an interface separation state need to overcome a larger energy barrier, and the bonding property of the GO-IBTS interface is stronger than that of the IBTS interface. Within 3050−3200 ps after interface separation, IBTS quickly reaches the equilibrium stage of IBTS double-sided stable adsorption, and the energy is stable and unchanged. However, the interaction energy of GO-IBTS increases stably with the increase of stretching distance because the single-sided functional group is detached from adsorption under the action of the stretching force. This phenomenon indicates that the amphiphilic property of IBTS makes the hydrophilic end produce surface adsorption with ettringite, while the hydrophobic end hinders the adsorption, resulting in relatively poor interfacial bonding performance of IBTS system. For the GO-IBTS system, there are polar functional groups on the GO surface to "bridge" the ettringite substrate, which improves the interface bonding performance.

4. CONCLUSIONS

In this work, the mechanism of interaction between silane and cement-based materials and the causes of interface bond failure under tensile force is studied by molecular dynamics simulation method to reveal the mechanism of GO modification of silane to improve interface bond performance from the molecular perspective. To further understand the mechanism and way of enhancing the macroscopic mechanical properties and guide the subsequent modification of sulfoaluminate cement-based materials, the specific conclusions are as follows:

(1) The interfacial-bonding properties of IBTS, GO-IBTS, and ettringite are derived from the bonding of ionic and hydrogen bonds between them. The modification of GO enhances the strength and stability of the Ca−O ionic bond formed by IBTS and ettringite. In addition, the three oxygen-containing functional groups on the surface of GO will also form a Ca−O ionic bond and hydrogen bond with ettringite, which is more stable than IBTS.

(2) In the tensile stage, the failure of the interface bond is due to the fracture of the ionic bond and hydrogen bond. The dynamic coordination number reflects the bond formation changes of the two systems during the tensile stage. The Ca−O ionic bond and hydrogen bond of the interface are broken due to the application of tensile force, which leads to the interface peeling. The tensile speed affects the force required to peel the interface. With the increase of the stretching speed, the force required by the two systems increases gradually. At the same tensile speed, the bond strength relationship of the two systems is GO-IBTS > IBTS.

(3) The bond strength between GO-IBTS and ettringite is greater than that of the IBTS system. In the stable adsorption state, the interaction energy between GO-IBTS and ettringite at the interface is lower than that of IBTS. The GO-IBTS system needs to overcome a larger energy barrier from the stable binding state to the interface separation state, and the bonding property of the GO-IBTS interface is stronger than that of the IBTS interface. In addition, the amphiphilicity of IBTS results in its interaction with unilateral ettringite, while the double-sided nature of GO's functional groups enables IBTS to interact well with bilateral ettringite, thus enhancing the interface-bonding performance.

AUTHOR INFORMATION

Corresponding Author

Pan Wang − *Department of Civil Engineering, Qingdao University of Technology, Qingdao 266033, China*; Email: wangpan@qut.edu.cn

Authors

Shaochun Li − *Department of Civil Engineering, Qingdao University of Technology, Qingdao 266033, China; Engineering Research Center of Concrete Technology under Marine Environment, Ministry of Education, Qingdao University of Technology, Qingdao 266033, China*

Yuying Duan − *Department of Civil Engineering, Qingdao University of Technology, Qingdao 266033, China*

Heping Zheng − *Department of Civil Engineering, Qingdao University of Technology, Qingdao 266033, China*; orcid.org/0000-0002-0959-4015

Dongshuai Hou − *Department of Civil Engineering, Qingdao University of Technology, Qingdao 266033, China*; orcid.org/0000-0002-1252-2987

Shiyu Sui − *Department of Civil Engineering, Qingdao University of Technology, Qingdao 266033, China*

Ang Liu − *Department of Civil Engineering, Qingdao University of Technology, Qingdao 266033, China*; orcid.org/0000-0001-5181-7094

Complete contact information is available at: https://pubs.acs.org/10.1021/acsomega.2c08123

Notes

The authors declare no competing financial interest.

ACKNOWLEDGMENTS

The authors acknowledge financial support from the National Natural Science Foundation of China under Grant Nos. 51978355, 52178221, and 51908308 and the Shandong Province Marine Environment Concrete Material Corrosion Control and Monitoring Research Innovation Team.

REFERENCES

(1) Qaidi, S. M.; Atrushi, D. S.; Mohammed, A. S.; Ahmed, H. U.; Faraj, R. H.; Emad, W.; Tayeh, B. A.; Najm, H. M. Ultra-high-performance geopolymer concrete: A review. *Constr. Build. Mater.* **2022**, *346*, No. 128495.

(2) Ahmed, H. U.; Mahmood, L. J.; Muhammad, M. A.; Faraj, R. H.; Qaidi, S. M.; Sor, N. H.; Mohammed, A. S.; Mohammed, A. A. Geopolymer concrete as a cleaner construction material: An overview on materials and structural performances. *Cleaner Mater.* **2022**, *5*, No. 100111.

(3) Thomas, B. S.; Gupta, R. C. A comprehensive review on the applications of waste tire rubber in cement concrete. *Renewable Sustainable Energy Rev.* **2016**, *54*, 1323−1333.

https://doi.org/10.1021/acsomega.2c08123
ACS Omega 2023, 8, 16016−16031

(4) Zhang, G.; Yang, Q.; Hou, D.; Zhou, P.; Ding, Q. Unraveling the microstructural properties of cement-slag composite pastes incorporated with smart polymer-based corrosion inhibitors: From experiment to molecular dynamics. *Cem. Concr. Compos.* **2022**, *125*, No. 104298.
(5) Dehwah, H. A.; Maslehuddin, M.; Austin, S. A. Long-term effect of sulfate ions and associated cation type on chloride-induced reinforcement corrosion in Portland cement concretes. *Cem. Concr. Compos.* **2002**, *24*, 17−25.
(6) Li, C.; Xiao-dong, G.; Li-ping, G.; Yun-feng, M.; Bao-sheng, H. Experimental studies on erosion mechanism of embankments subjected to wind and freeze-thaw compound erosion in cold and arid regions. *Eng. Mech.* **2015**, *32*, 177−182.
(7) Liu, J.; Zhang, W.; Li, Z.; Jin, H.; Tang, L. Influence of deicing salt on the surface properties of concrete specimens after 20 years. *Constr. Build. Mater.* **2021**, *295*, No. 123643.
(8) Liu, F.; Zhang, T.; Luo, T.; Zhou, M.; Zhang, K.; Ma, W. Study on the Deterioration of Concrete under Dry−Wet Cycle and Sulfate Attack. *Materials* **2020**, *13*, 4095.
(9) Liu, X.; Ma, E.; Liu, J.; Zhang, B.; Niu, D.; Wang, Y. Deterioration of an industrial reinforced concrete structure exposed to high temperatures and dry-wet cycles. *Eng. Failure Anal.* **2022**, *135*, No. 106150.
(10) Pradhan, B. Corrosion behavior of steel reinforcement in concrete exposed to composite chloride−sulfate environment. *Constr. Build. Mater.* **2014**, *72*, 398−410.
(11) Shaheen, F.; Pradhan, B. Influence of sulfate ion and associated cation type on steel reinforcement corrosion in concrete powder aqueous solution in the presence of chloride ions. *Cem. Concr. Res.* **2017**, *91*, 73−86.
(12) Li, C. Q. Initiation of chloride-induced reinforcement corrosion in concrete structural members—experimentation. *ACI Struct. J.* **2001**, *98*, 502−510.
(13) Lu, L.; Li, X.; Zhou, J. *Study of damage to a high concrete dam subjected to underwater shock waves* **2014**, *13*, 337−346.
(14) Gálvez-Martos, J.-L.; Styles, D.; Schoenberger, H.; Zeschmar-Lahl, B. Construction and demolition waste best management practice in Europe. *Resour., Conserv. Recycl.* **2018**, *136*, 166−178.
(15) Bansal, S.; Singh, S. A sustainable approach towards the construction and demolition waste. *Int. J. Innovative Res. Sci. Eng. Technol.* **2014**, *3*, 1262−1269.
(16) Wang, S. Cementation and expansion performance of sulphoaluminate cement based compound system. *Cement* **2018**, *06*, 1−6.
(17) Liu, C.; Luo, J.; Li, Q.; Gao, S.; Jin, Z.; Li, S.; Zhang, P.; Chen, S. Water-resistance properties of high-belite sulphoaluminate cement-based ultra-light foamed concrete treated with different water repellents. *Constr. Build. Mater.* **2019**, *228*, No. 116798.
(18) Guo, L.; Guan, H.; Yang, X. Effect of methylsilane waterproof agent on frost resistance of foam concrete. *J. Harbin Eng. Univ.* **2018**, *39*, 2075−2079.
(19) Chen, H.; Guo, Z.; Hou, P.; Fu, X.; Qu, Y.; Li, Q.; Cheng, X.; Zhu, X. The influence of surface treatment on the transport properties of hardened calcium sulfoaluminate cement-based materials. *Cem. Concr. Compos.* **2020**, *114*, No. 103784.
(20) Zhang, C.; Zhang, S.; Yu, J.; Kong, X. Water absorption behavior of hydrophobized concrete using silane emulsion as admixture. *Cem. Concr. Res.* **2022**, *154*, No. 106738.
(21) Li, H.; Xu, C.; Dong, B.; Chen, Q.; Gu, L.; Yang, X. Enhanced performances of cement and powder silane based waterproof mortar modified by nucleation CSH seed. *Constr. Build. Mater.* **2020**, *246*, No. 118511.
(22) Feng, Z.; Wang, F.; Xie, T.; Ou, J.; Xue, M.; Li, W. Integral hydrophobic concrete without using silane. *Constr. Build. Mater.* **2019**, *227*, No. 116678.
(23) Zhu, Y.-G.; Kou, S.-C.; Poon, C.-S.; Dai, J.-G.; Li, Q.-Y. Influence of silane-based water repellent on the durability properties of recycled aggregate concrete. *Cem. Concr. Compos.* **2013**, *35*, 32−38.
(24) Zhang, Y.; Li, S.; Zhang, W.; Chen, X.; Hou, D.; Zhao, T.; Li, X. Preparation and mechanism of graphene oxide/isobutyltriethoxysilane composite emulsion and its effects on waterproof performance of concrete. *Constr. Build. Mater.* **2019**, *208*, 343−349.
(25) Shi, D.; Geng, Y.; Li, S.; Gao, J.; Hou, D.; Jin, Z.; Liu, A. Efficacy and mechanism of graphene oxide modified silane emulsions on waterproof performance of foamed concrete. *Case Stud. Constr. Mater.* **2022**, *16*, No. e00908.
(26) Chen, X.; Zhang, Y.; Li, S.; Geng, Y.; Hou, D. Influence of a new type of graphene oxide/silane composite emulsion on the permeability resistance of damaged concrete. *Coatings* **2021**, *11*, 208.
(27) Gao, J.; Geng, Y.; Li, S.; Chen, X.; Shi, D.; Zhou, P.; Zhou, Z.; Wu, Z. Effect of silane emulsion on waterproofing and Anti-icing performance of foamed concrete. *Constr. Build. Mater.* **2021**, *301*, No. 124082.
(28) Zhang, Y.; Li, S.; Hou, D.; Xiao, Q. Effect of GO / Silane Composite Emulsion on Impermeability of Concrete. *Paint Coat. Ind.* **2018**, *48*, 13−18.
(29) Li, S.; Liu, J.; Geng, Y.; Liu, A.; Xu, A.; Hou, D.; Lang, X. Efficacy and mechanism of GO/IBTS coating against microbial fouling of concrete surfaces in marine tidal areas. *J. Coat. Technol. Res.* **2022**, *19*, 875−885.
(30) Hou, D.; Yu, J.; Wang, P. Molecular dynamics modeling of the structure, dynamics, energetics and mechanical properties of cement-polymer nanocomposite. *Composites, Part B* **2019**, *162*, 433−444.
(31) Wang, P.; Yang, Q.; Wang, M.; Hou, D.; Jin, Z.; Wang, P.; Zhang, J. Theoretical investigation of epoxy detachment from CSH interface under aggressive environment. *Constr. Build. Mater.* **2020**, *264*, No. 120232.
(32) Zhou, Y.; Huang, J.; Yang, X.; Dong, Y.; Feng, T.; Liu, J. Enhancing the PVA fiber-matrix interface properties in ultra high performance concrete: An experimental and molecular dynamics study. *Constr. Build. Mater.* **2021**, *285*, No. 122862.
(33) Liu, Z.; Xu, D.; Gao, S.; Zhang, Y.; Jiang, J. Assessing the adsorption and diffusion behavior of multicomponent ions in saturated calcium silicate hydrate gel pores using molecular dynamics. *ACS Sustainable Chem. Eng.* **2020**, *8*, 3718−3727.
(34) Zhang, W.; Zhang, M.; Hou, D. Nanoscale insights into the anti-erosion performance of concrete: A molecular dynamics study. *Appl. Surf. Sci.* **2022**, *593*, No. 153403.
(35) Wu, W.; Al-Ostaz, A.; Cheng, A. H.-D.; Song, C. R. Computation of elastic properties of Portland cement using molecular dynamics. *J. Nanomech. Micromech.* **2011**, *1*, 84−90.
(36) Bauchy, M. Structural, vibrational, and elastic properties of a calcium aluminosilicate glass from molecular dynamics simulations: the role of the potential. *J. Chem. Phys.* **2014**, *141*, No. 024507.
(37) Zhang, Y.; Zhou, Q.; Ju, J. W.; Bauchy, M. New insights into the mechanism governing the elasticity of calcium silicate hydrate gels exposed to high temperature: a molecular dynamics study. *Cem. Concr. Res.* **2021**, *141*, No. 106333.
(38) Wang, M.; Zhang, K.; Ji, X.; Wang, P.; Ma, H.; Zhang, J.; Hou, D. Molecular insight into the fluidity of cement pastes: Nano-boundary lubrication of cementitious materials. *Constr. Build. Mater.* **2022**, *316*, No. 125800.
(39) Hou, D.; Zheng, H.; Wang, P.; Wan, X.; Wang, M.; Wang, H. Molecular insight in the wetting behavior of nanoscale water droplet on CSH surface: Effects of Ca/Si ratio. *Appl. Surf. Sci.* **2022**, *587*, No. 152811.
(40) Hou, D.; Zheng, H.; Duan, Y.; Wang, P.; Wan, X.; Yin, B.; Wang, M.; Wang, X. Understanding the wetting discrepancy in calcium alumino silicate hydrate induced by Al/Si ratio. *Phys. Chem. Chem. Phys.* **2022**, *24*, 6973−6987.
(41) Bauchy, M.; Laubie, H.; Qomi, M. A.; Hoover, C.; Ulm, F.-J.; Pellenq, R.-M. Fracture toughness of calcium−silicate−hydrate from molecular dynamics simulations. *J. Non-Cryst. Solids* **2015**, *419*, 58−64.
(42) Bauchy, M. Structural, vibrational, and thermal properties of densified silicates: Insights from molecular dynamics. *J. Chem. Phys.* **2012**, *137*, No. 044510.
(43) Hou, D.; Li, T.; Han, Q.; Zhang, J. Insight on the sodium and chloride ions adsorption mechanism on the ettringite crystal: Structure,

https://doi.org/10.1021/acsomega.2c08123
ACS Omega 2023, 8, 16016−16031

dynamics and interfacial interaction. *Comput. Mater. Sci.* **2018**, *153*, 479−492.
(44) Moore, A. E.; Taylor, H. Crystal structure of ettringite. *Acta Crystallogr., Sect. B* **1970**, *26*, 386−393.
(45) Qian, J.; Yu, J.; Sun, H.; Ma, Y. Formation and function of ettringite in cement hydrates. *J. Chin. Ceram. Soc.* **2017**, *45*, 1569−1581.
(46) Cygan, R. T.; Liang, J.-J.; Kalinichev, A. G. Molecular models of hydroxide, oxyhydroxide, and clay phases and the development of a general force field. *J. Phys. Chem. B* **2004**, *108*, 1255−1266.
(47) Honorio, T.; Guerra, P.; Bourdot, A. Molecular simulation of the structure and elastic properties of ettringite and monosulfoaluminate. *Cem. Concr. Res.* **2020**, *135*, No. 106126.
(48) Plimpton, S.; Crozier, P.; Thompson, A. LAMMPS − large-scale atomic/molecular massively parallel simulator. *Soft Nanosci. Lett.* **2007**, *18*, 43.
(49) Nosé, S. A unified formulation of the constant temperature molecular dynamics methods. *J. Chem. Phys.* **1984**, *81*, 511−519.
(50) Keil, F. J. Multiscale modelling in computational heterogeneous catalysis. *Top. Curr. Chem.* **2012**, *307*, 69−107.
(51) Evans, D. J.; Hoover, W. G.; Failor, B. H.; Moran, B.; Ladd, A. J. Nonequilibrium molecular dynamics via Gauss's principle of least constraint. *Phys. Rev. A* **1983**, *28*, 1016.
(52) Wang, P.; Yang, Q.; Jin, Z.; Hou, D.; Wang, M. Effects of water and ions on bonding behavior between epoxy and hydrated calcium silicate: a molecular dynamics simulation study. *J. Mater. Sci.* **2021**, *56*, 16475−16490.
(53) Duan, Y.; Zheng, H.; Wang, P.; Hou, D.; Wang, M.; Yin, B.; Li, S. Molecular dynamics simulation study on the hydrophobic mechanism of Ettringite nanoporous channels modified by silane and silane/graphene oxide. *Appl. Surf. Sci.* **2023**, *623*, No. 156975.

https://doi.org/10.1021/acsomega.2c08123
ACS Omega 2023, 8, 16016−16031